

Supporting Information

Effect of Intercalated Alkali Ions in Layered Manganese Oxide Nanosheets as Neutral Electrochemical Capacitors

Nattapol Ma^a, Soracha Kosasang^a, Atiweena Krittayavathananon^a, Nutthaphon Phattharasupakun^a,
Sethuraman Sathyamoorthi^a and Montree Sawangphruk^{*a}

^aCentre of Excellence for Energy Storage Technology (CEST), Department of Chemical and Biomolecular
Engineering, School of Energy Science and Engineering, Vidyasirimedhi Institute of Science and
Technology, Rayong 21210, Thailand

*Corresponding author. Tel: +66(0)33-01-4251 Fax: + 66(0)33-01-4445.

E-mail address: montree.s@vistec.ac.th (M. Sawangphruk).

ORCID ID: <https://orcid.org/0000-0003-2769-4172>

Experimental Section

Chemicals and Materials

Manganese(II) nitrate tetrahydrate ($\text{Mn}(\text{NO}_3)_2 \cdot 4\text{H}_2\text{O}$, 98%, Loba Chemie), Lithium hydroxide (LiOH, 98%, Sigma-Aldrich), Sodium hydroxide (NaOH, 99.8%, Ajax Finechem), Potassium hydroxide (KOH, Ajax Finechem), Hydrogen peroxide (H_2O_2 , 30%, Chem Merck), Polyvinylidene fluoride (PVDF, $M_w \sim 534,000$, Sigma-Aldrich), Sodium sulphate (Na_2SO_4 , Univar), Acetylene black (TIMCAL), N-Methyl-2-pyrrolidone (NMP, 99.5%, Qrec), Polytetrafluoroethylene preparation (PTFE, 60 wt % dispersion in H_2O , Sigma-Aldrich), and Ethanol ($\text{C}_2\text{H}_5\text{OH}$, 99.5%, Sigma-Aldrich) are analytical grade and used without further purification. Nickel foam (200 g m^{-2} with a thickness of 1mm, Gelon) and carbon fiber paper (CFP, SGL CARBON SE, Germany) were used as substrate. Deionized water was purified by using Milli-Q system (DI water, $15 \text{ M}\Omega \cdot \text{cm}$, Millipore).

Synthesis of Birnessite Manganese oxide

The birnessite-type manganese oxide with X^+ , ($X^+ = \text{Li}^+, \text{Na}^+, \text{or K}^+$), as a structural (intercalated) cation ($X\text{-MnO}_x$) was prepared via the addition of 100 mL solution of 0.6 M $X\text{OH}\cdot\text{H}_2\text{O}$ and 1 M H_2O_2 to 60 mL of 0.25 M $\text{Mn}(\text{NO}_3)_2\cdot 4\text{H}_2\text{O}$. After stirring at room temperature for 1 h, a dark brown precipitate was observed. The precipitate was then filtered and washed with DI water to remove impurities. The obtained product was dried at 50 °C for 48 h. Note, $X\text{OH}\cdot\text{H}_2\text{O}$ are $\text{LiOH}\cdot\text{H}_2\text{O}$, $\text{NaOH}\cdot\text{H}_2\text{O}$, and $\text{KOH}\cdot\text{H}_2\text{O}$ for Li-MnO_x , Na-MnO_x , and K-MnO_x respectively.^{1, 2}

Morphological and structural characterizations

The morphologies and surface composition of the as-synthesized layered manganese oxide (birnessite) were investigated via Field-Emission Scanning Electron Microscopy (FE-SEM, JSM-7001F, JEOL Ltd.), Energy Dispersive X-ray Spectroscopy (EDX, Oxford Instruments), and Transmission electron microscopy (TEM, JEOL Ltd., Japan). X-ray powder diffraction (XRD) patterns were acquired using D8 ADVANCE with DAVINCI design (Bruker, $\text{CuK}\alpha$ of 1.5418 Å). The chemical structure of the samples was investigated by Raman spectroscopy (Senterra Dispersive Raman Microscope, Bruker). *In situ* Mn K-edge fluorescent X-ray absorption spectroscopy (XAS) was characterized at Synchrotron Light Research Institute BL. 5.2 (Public Organization), Thailand. Note, XAS has equipped with Ge (220) double-crystal monochromator with an energy range of 3440-12100 eV. The C:Mn ratios were obtained from Inductively coupled plasma - optical emission spectrometry (ICP-OES, Agilent Technologies 700 series).

Electrochemical evaluation

In this work, electrochemical evaluation was performed using a three-electrode configuration in 1 M Na_2SO_4 electrolyte with platinum wire and saturated calomel electrode (SCE) as counter and reference electrodes, respectively. Nickel foam current collector was first washed with ethanol and pressed using a roller mill to obtain a 0.2 mm thick sheet, then cut into a $1\times 1\text{ cm}^2$ sheet. The electrodes were prepared by mixing active material (Li-MnO_x , Na-MnO_x , or K-MnO_x) with acetylene black (conductive material) and PTFE (binder) with a weight ratio of 6:3:1 in ethanol. The slurry was ground continuously to form a freestanding dough like pastes. The 1 cm^2 freestanding sheet with an active mass of $\sim 3\text{ mg}$ was then uniformly pasted over the nickel foam current collector and dried in a vacuum oven at 60°C for 24

h. The electrochemical properties were evaluated by cyclic voltammetry (CV), galvanostatic charge/discharge (GCD), and electrochemical impedance spectroscopy (EIS) using Metrohm AUTOLAB potentiostat (PGSTAT302N). Note, the stability test was performed using the GCD technique at 3 A g⁻¹.

The specific capacitance (C_{cv}) was obtained from CV results via the following equation (S1)³⁻⁶;

$$C_{cv} = \frac{\int IdV/v}{m\Delta V} \quad (S1)$$

where $\int IdV/v$ is a total amount of charge that involved in the discharge process (Coulomb) of CV curve, ΔV is the working potential (versus SCE) determined from the discharge potential window (V), and m is the total mass of active material used in each electrode (g, 60% of total mass per electrode).

The specific capacitance (C_{GCD}) was calculated from the GCD technique by following equation (S2)^{4, 5, 7};

$$C_{GCD} = \frac{I\Delta t}{\Delta Vm} \quad (S2)$$

where I is the applied current (A), Δt is the discharging time (s), and ΔV is the working potential window (versus SCE) excluding the iR drop.

The specific capacitance from EIS technique (C_{EIS}) can also be calculated from equation (S3)^{8, 9};

$$C_{EIS} = \frac{-1}{2\pi fZ''m} \quad (S3)$$

where f is the frequency applied and Z'' is the imaginary component of the impedance at that applied frequency.

Relaxation time constant (τ_0) or dielectric relaxation time for supercapacitor. The parameter represents the transition of electrochemical capacitor behavior from ideal resistor to ideal

capacitor or a minimum time required for fully discharging all the stored charges. The τ_0 is calculated from $\tau_0 = 1/(2\pi f_0)$, where f_0 is a crossing frequency (also denote as resonance frequency) of the plots between $|P|/|S|$ and $|Q|/|S|$ in the complex power analysis diagram (normalized complex power vs. frequency), where $P(\omega)$, $Q(\omega)$, and $S(\omega)$ were calculated using equation (S4 – S8)^{7, 10}.

$$P(\omega) = \omega C''(\omega) |\Delta V_{rms}|^2 \quad (S4)$$

$$Q(\omega) = -\omega C'(\omega) |\Delta V_{rms}|^2 \quad (S5)$$

$$S(\omega) = P(\omega) + jQ(\omega) \quad (S6)$$

$$C'(\omega) = -Z''(\omega) / \{\omega |Z(\omega)|^2\} \quad (S7)$$

$$C''(\omega) = Z'(\omega) / \{\omega |Z(\omega)|^2\} \quad (S8)$$

where $|\Delta V_{rms}|^2 = \Delta V_{max} / \sqrt{2}$ (V_{max} represents the maximum amplitude of the ac signal), j is imaginary number, and $\omega = 2\pi f$ (angular frequency). The Z' and Z'' represent real and imaginary parts of the complex impedance Z .

The sweep-rate dependences of voltammetric currents can quantitatively distinguish the capacitance contribution with respect to the response current. The response current could be differentiated to surface mechanism and the diffusion-controlled process via equation (S9)¹¹⁻¹⁵;

$$i(V) = k_1 v + k_2 v^{0.5} \quad (S9)$$

where $k_1 v$ and $k_2 v^{0.5}$ represent the surface mechanism and diffusion-controlled effect, respectively.

The rotating disk electrode (RDE) measurement in a three-electrode system in 1 M Na₂SO₄ was utilized to study the heterogeneous rate constant of electron transfer (k_0 , cm s⁻¹). 50 mg mixture of 60% active material, 30% acetylene black, and 10% PVDF was dissolved in 200 μ L NMP and sonicated for 3 h. 2.5 μ L of the obtained mixture was dropped on a 3-mm glassy carbon rotating disk electrode (GC-RDE) and dried in an ambient environment. The coated GC-RDE, platinum rod, and SCE were used as the working electrode, counter electrode, and reference electrode, respectively. The EIS analysis was carried out in

a frequency range of 100 Hz to 1 MHz with an applied potential of 0.01 V. The k_0 is obtained by equation (S10).

$$k_0 = \frac{RT}{nF^2 A C_s R_{ct}}$$

(S10)

where R is the gas constant, T is the absolute temperature (K), n is the number of electrons involved in the reaction, C_s is the bulk concentration, and R_{ct} is the charge transfer resistance (Ω).

In situ X-ray adsorption spectroscopy (In situ XAS)

The oxidation state of Mn under charging (from -0.1 to 0.8 V versus SCE) and discharging process (from 0.8 to -0.1 V versus SCE) was studied via coupling of *in situ* K-edge XAS measurement with chronoamperometry. The measurement was performed with a three-electrode set up using coated CFP (with the same ink in RDE measurement), platinum rod, and SCE as working, counter, and reference electrode respectively. Note, the test cell with the dimension of 2 cm \times 2 cm \times 3.5 cm was fabricated from acrylic sheets with a square opening space on one of the 2-cm² sides (covered by a Kapton tape). Reference and counter electrodes were placed alongside with the working electrode at ca. 1 cm (out of X-rays range). *In situ* measurement was performed at a steady-state current by holding the working electrode at a specific potential of interest for at least 15 min before each measurement.¹⁶⁻¹⁸

The oxidation state of Mn can be calculated using an empirical equation when located between Mn⁴⁺ and Mn³⁺ (S11)¹⁹⁻²¹.

$$\text{Oxidation state of Mn} = 4 \left(\frac{\Delta E \text{ of sample}}{\Delta E \text{ of Mn}^{3+} \text{ and Mn}^{4+}} \right) + 3 \left(1 - \frac{\Delta E \text{ of sample}}{\Delta E \text{ of Mn}^{3+} \text{ and Mn}^{4+}} \right)$$

(S11)

Electrochemical quartz crystal microbalance (EQCM)

To study the resulting mass changes, Δm , of the Li-MnO_x, Na-MnO_x, and K-MnO_x an *in situ* gravimetric monitoring via EQCM method. To prepare the EQCM electrode, 30 mg of active material was dispersed in 200 μ L NMP and sonicated for 3 h then drop-coating onto the Au/TiO₂ quartz crystal electrode (20 μ L per electrode). The *in situ* gravimetric monitoring together with linear sweep measurements at 40 mV s⁻¹ in 1 M Na₂SO₄ was conducted in three-electrode configuration with Ag/AgCl (3M KCl) and gold wire as reference and counter electrode, respectively. The mass change (Δm) can be obtained from the quartz resonance frequency (Δf) via Sauerbrey equation (S12). Note, calibration constant (C_f) is 0.0815 Hz ng⁻¹cm².^{22, 23}

$$\Delta f = -C_f \Delta m \quad (\text{S12})$$

Additional figures

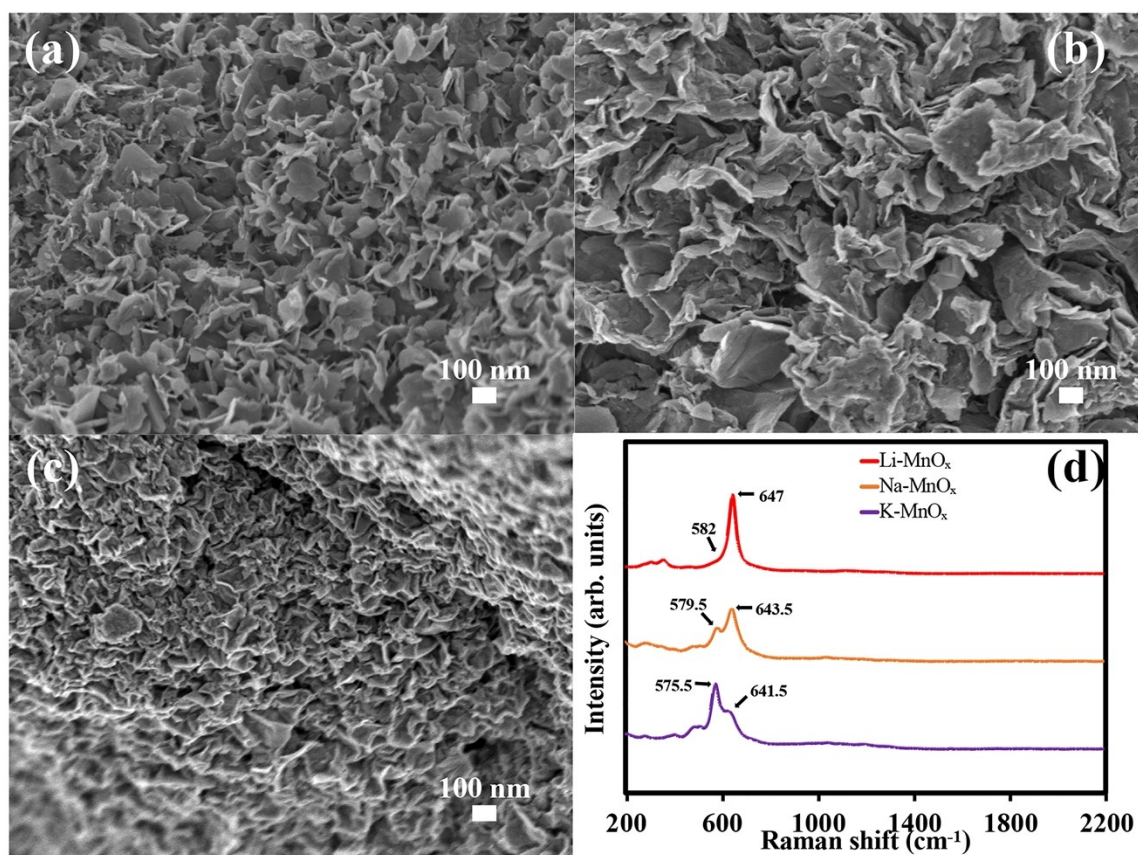


Figure S1. SEM images of birnessite-type layered manganese oxides (δ -MnO_x); (a) Li-MnO_x, (b) Na-MnO_x, (c) K-MnO_x, and (d) their Raman spectra.

The morphologies of the as-synthesized birnessite manganese oxides were first investigated using field emission-scanning electron microscopy (FE-SEM). All birnessite samples display organized sheet-like pattern with an average sheet thickness of ca. 5 nm (Figure S1a-c). The Raman spectra (Figure S1d) reveal the characteristic vibration of δ -MnO₂ between 300-647 cm⁻¹. The contribution could be divided into stretching vibration (644-647 cm⁻¹), stretching on the basal plane (509-582 cm⁻¹), and Mn-O bending vibration (307-358 cm⁻¹).^{24, 25}

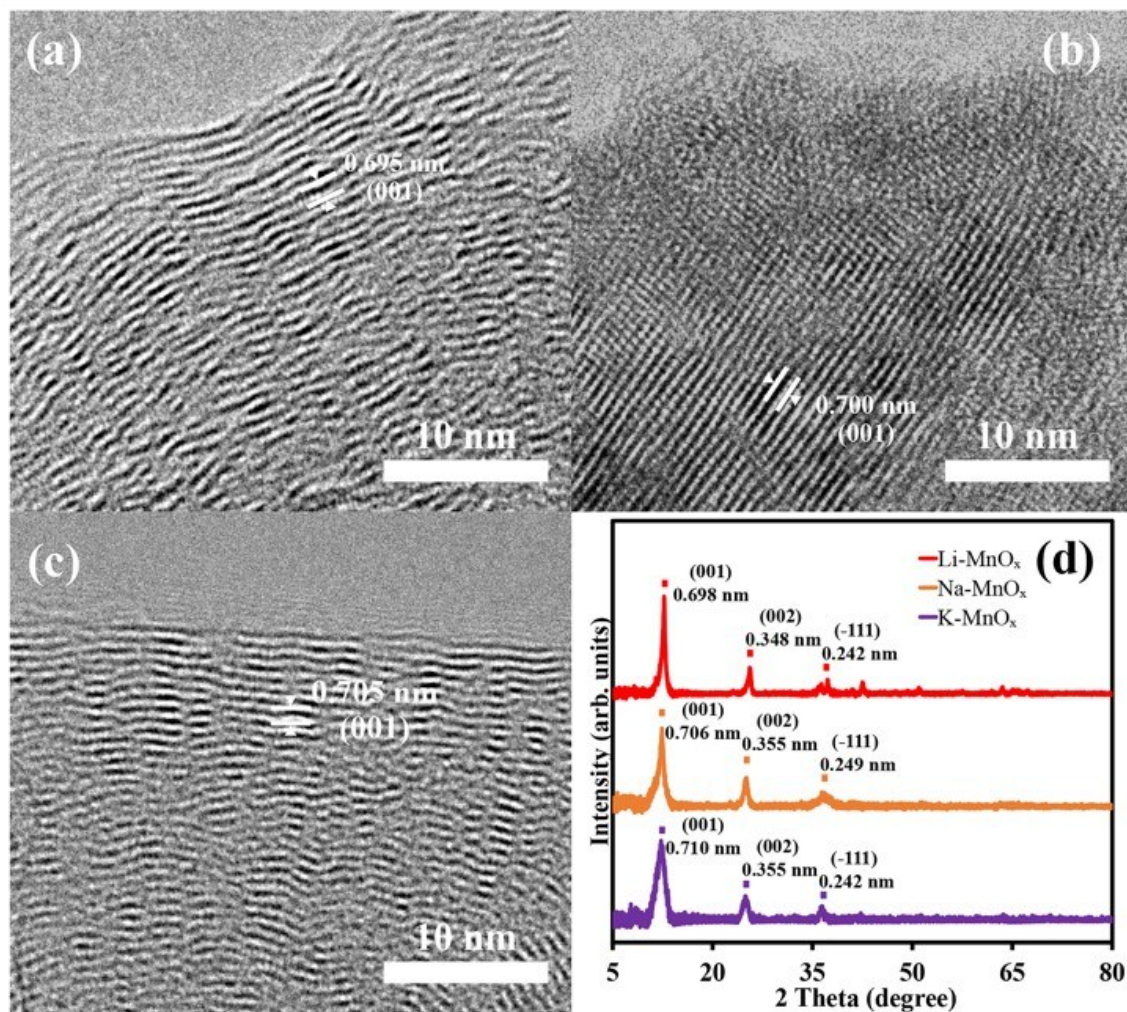


Figure S2. TEM images of birnessite-type layered manganese oxides (δ -MnO_x); (a) Li-MnO_x, (b) Na-MnO_x, (c) K-MnO_x, and (d) their XRD patterns.

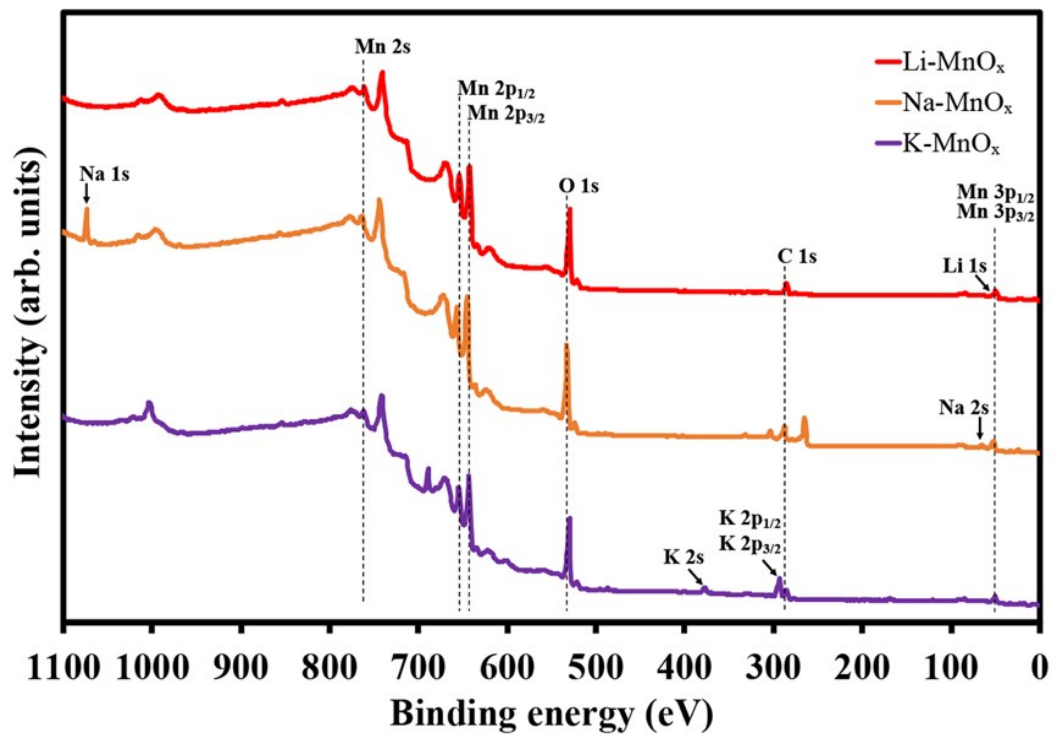


Figure S3. Wide-scan XPS spectra of Li-MnO_x, Na-MnO_x, and K-MnO_x.

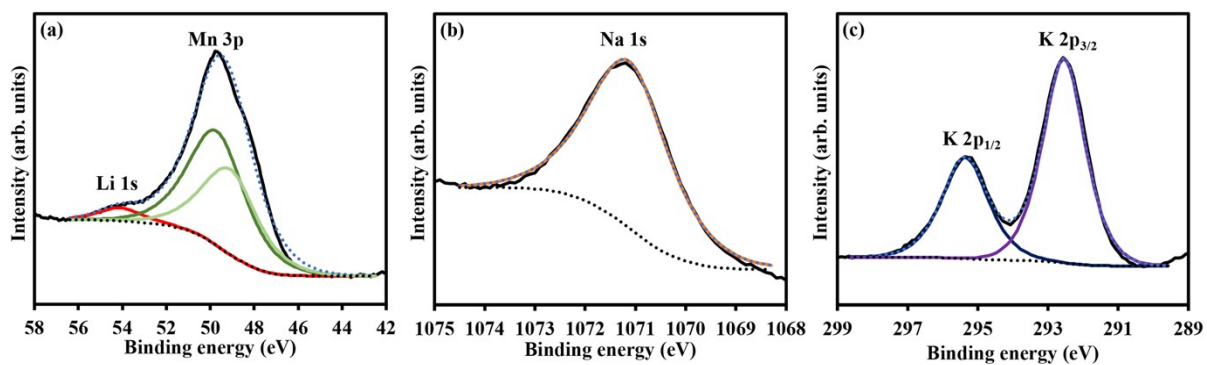


Figure S4. XPS spectra of (a) Li 1s of Li-MnO_x, (b) Na 1s of Na-MnO_x, and (c) K 2p of K-MnO_x.

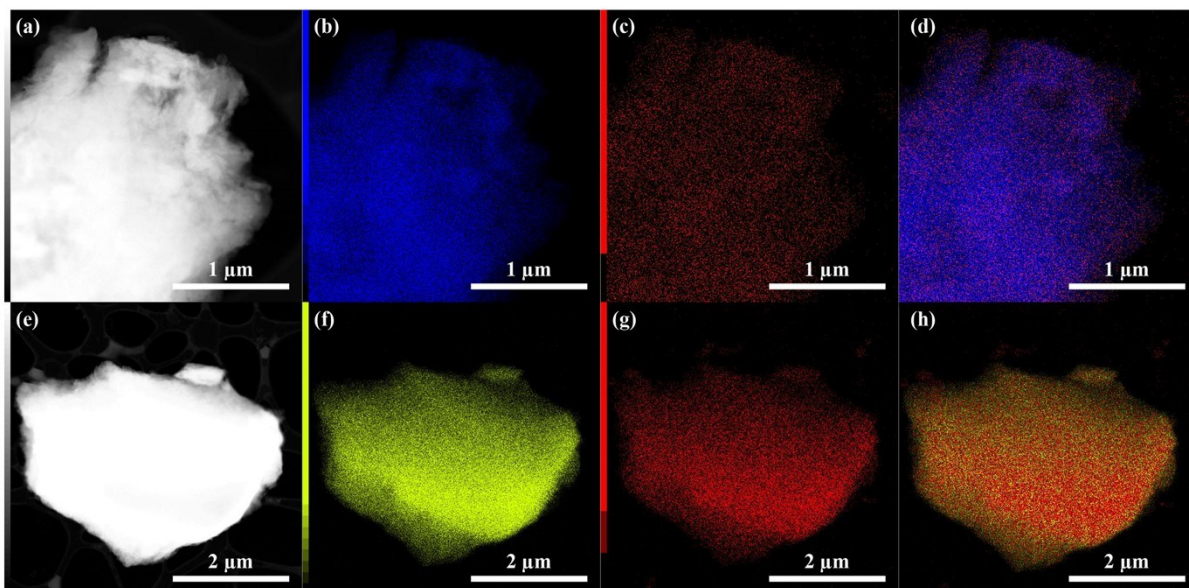


Figure S5. EDS mapping showing (a) STEM, (b) manganese, (c) sodium, and (d) overlay mapping of manganese and sodium of Na-MnO_x as well as (e) STEM, (f) manganese, (g) potassium, and (h) overlay mapping of manganese and potassium of K-MnO_x.

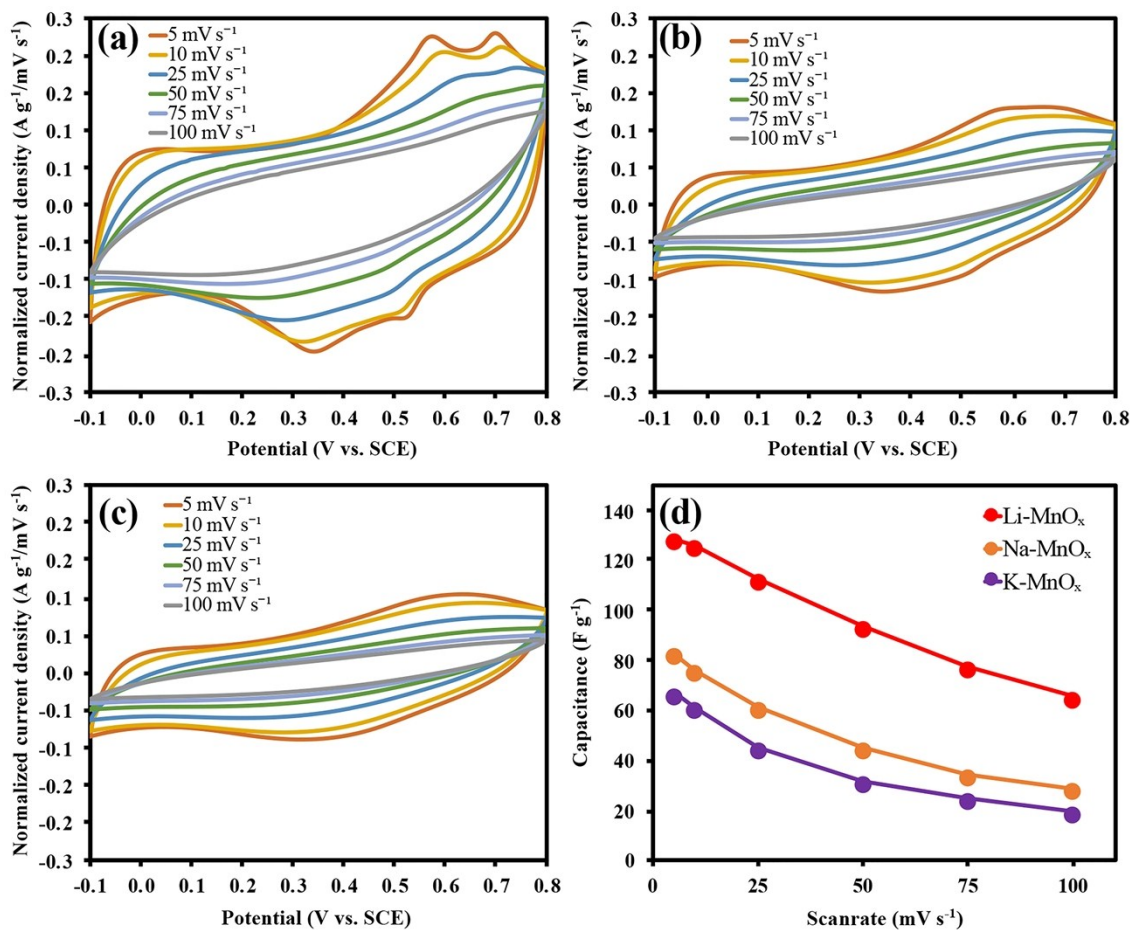


Figure S6. CVs at different scan rates of (a) Li-MnO_x, (b) Na-MnO_x, and (c) K-MnO_x as well as (d) their specific capacitance as a function of scan rates.

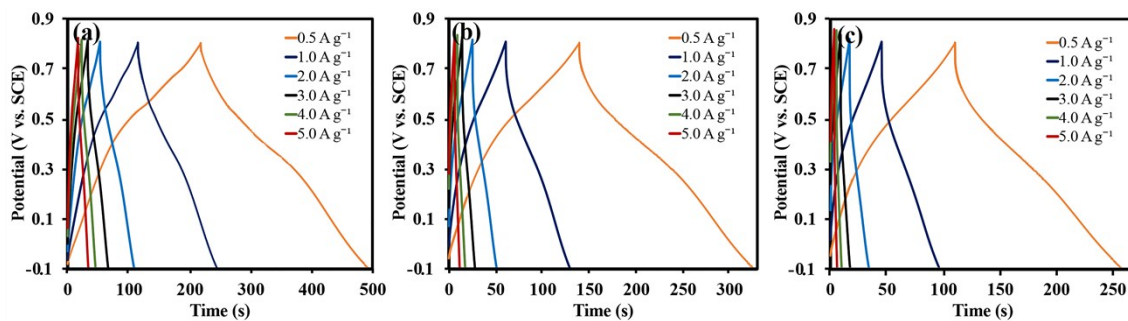


Figure S7. GCDs at different scan rates of (a) Li-MnO_x, (b) Na-MnO_x, and (c) K-MnO_x.

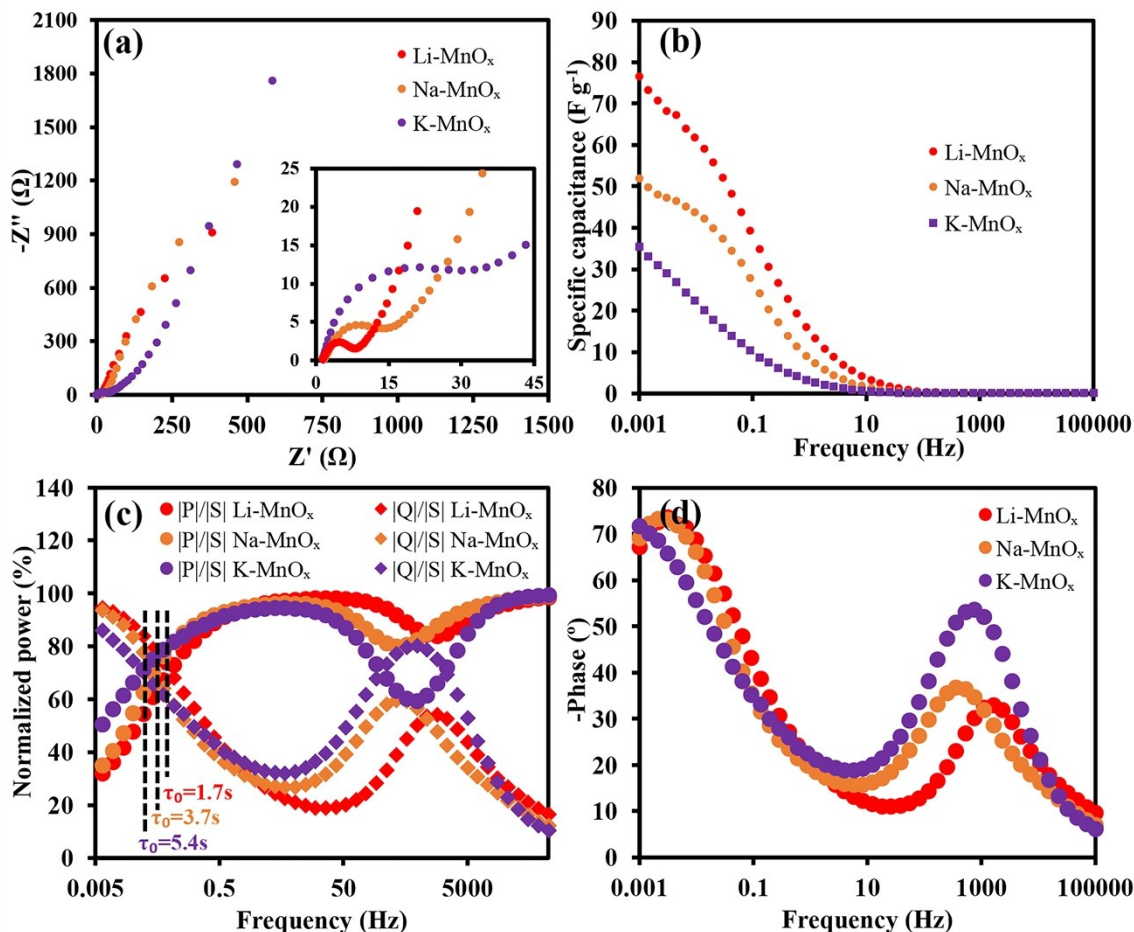


Figure S8. (a) Nyquist plots, (b) Specific capacitance calculated from EIS measurements, (c) complex power analysis, and (d) Bode plot of Li-MnO_x, Na-MnO_x, and K-MnO_x.

Electrochemical impedance spectroscopy (EIS) of all samples was further studied to probe the effect of structural cations on the intercalation process of the electrolyte ions. Figure S8a shows Nyquist plots of the birnessite with different structural cations. The charge transfer resistance (R_{ct}) increases in the order of Li-MnO_x (7.1Ω) < Na-MnO_x (14.2 Ω) < K-MnO_x (29.5 Ω). The increase of R_{ct} implies that the Na⁺ diffusion becomes more difficult as the ionic size of the available structural ion increases.²⁶ The specific capacitances calculated from EIS at an applied frequency of 1 mHz (Figure S8b) are 305, 208, and 141 F g⁻¹ for Li-MnO_x, Na-MnO_x and K-MnO_x, respectively. The response frequency or relaxation time (τ_0) was obtained from the resonance frequency of the complex power analysis diagram in Figure S8c. The τ_0 represents the transition time from resistive to capacitive behavior or the minimum time required to dissipate a half of the stored charge. Li-MnO_x exhibits a smallest τ_0 of 1.7s followed by Na-MnO_x (3.7s) and K-MnO_x (5.4s).²⁷ This could further indicate the effect of structural cations on the diffusion capability of the electrolytic ions to the available sites.¹⁰ As presented in the Bode phase diagram (Figure S8d), the

Li-MnO_x shows the highest faradaic characteristic as the phase shift at low-frequency region shows the highest deviation from the 90° (67.1°) followed by Na-MnO_x, (70.0°) and K-MnO_x (71.6°).

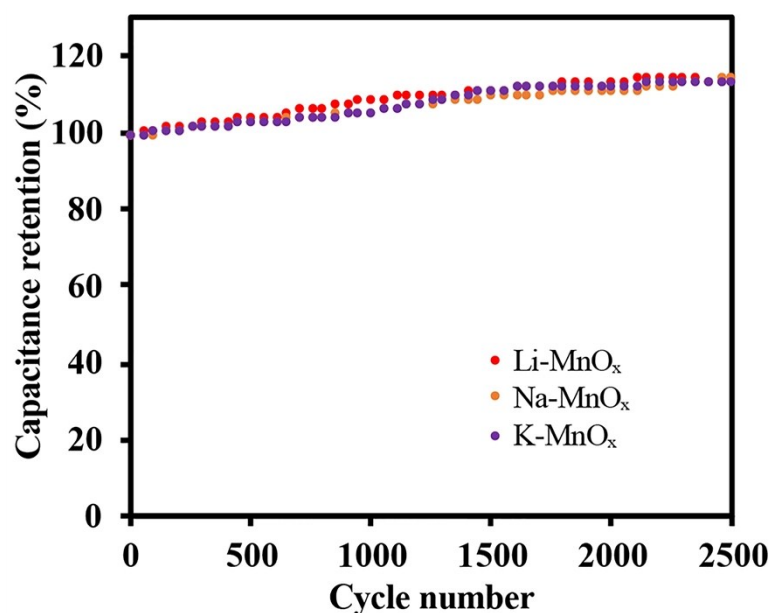


Figure S9. (a) Stability test of Li-MnO_x, Na-MnO_x, and K-MnO_x at 3 A g⁻¹.

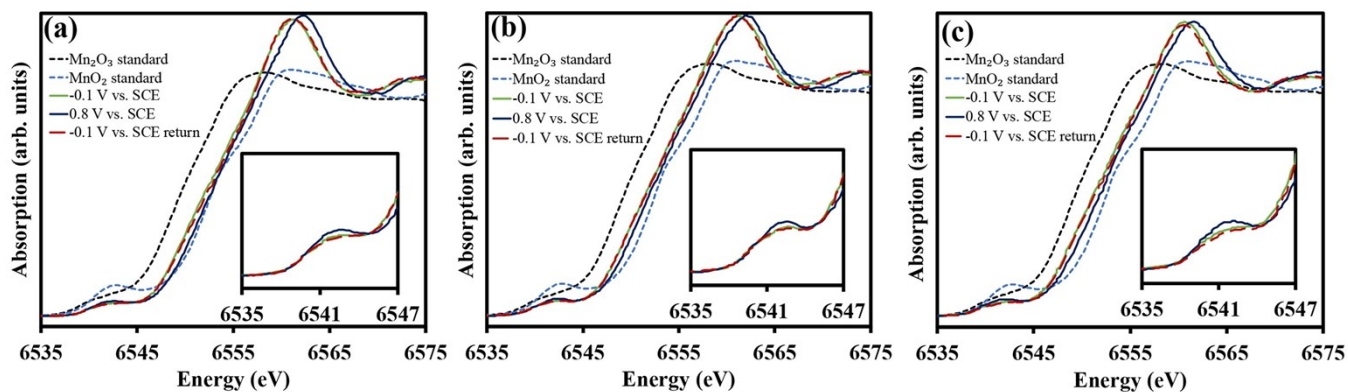


Figure S10. *In situ* Mn K-edge XANES spectra at different applied potential for (a) Li-MnO_x, (b) Na-MnO_x, and (c) K-MnO_x.

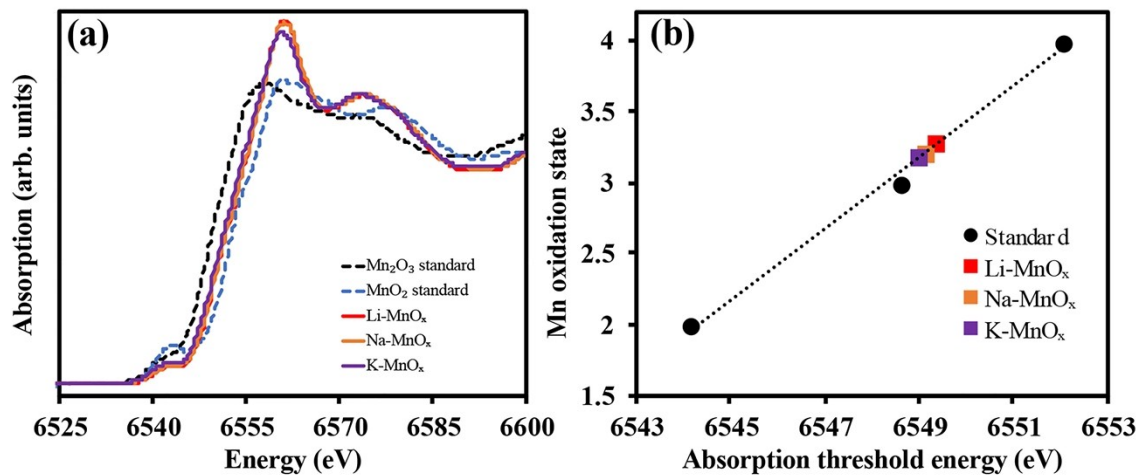


Figure S11. (a) *In situ* Mn K-edge XANES spectra and (b) the Mn oxidation state derived from XAS measurement of Li-MnO_x, Na-MnO_x and K-MnO_x.

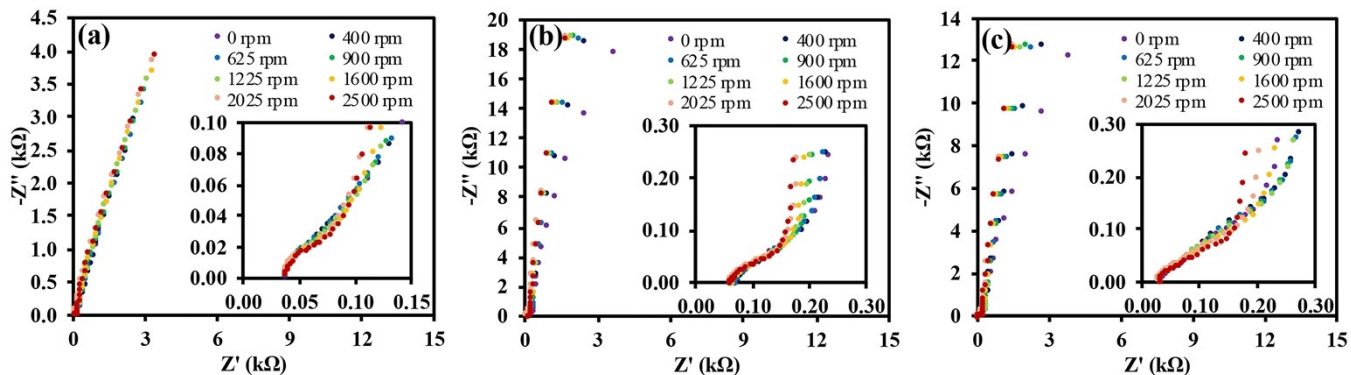


Figure S12. Nyquist plots of (a) Li-MnO_x, (b) Na-MnO_x, and (c) K-MnO_x coated on glassy carbon rotating electrode (GC-RDE) at different rotation rates.

The EIS was also performed at different rotation rates of 0, 400, 625, 900, 1225, 1600, 2025, and 2500 rpm, which are shown as Nyquist plots in Figure S12a-c. In addition, the equivalent circuit obtained by EIS fitting process is given in Figure S12d. When the rotation rate increases, the R_{ct} slightly decreases due to the contribution of forced convection between the bulk electrolyte and the electroactive surface. At low-frequency region, a clear shift toward the y-axis was observed, due to a better electrolyte ion-diffusion process for in K-MnO_x and Na-MnO_x. Also, the more pronounced shift was noted with increasing the rotation rates. However, the curve at low-frequency region was slightly shifted for Li-MnO_x, confirming the superiority in term of ion diffusion as observed in the previous section.

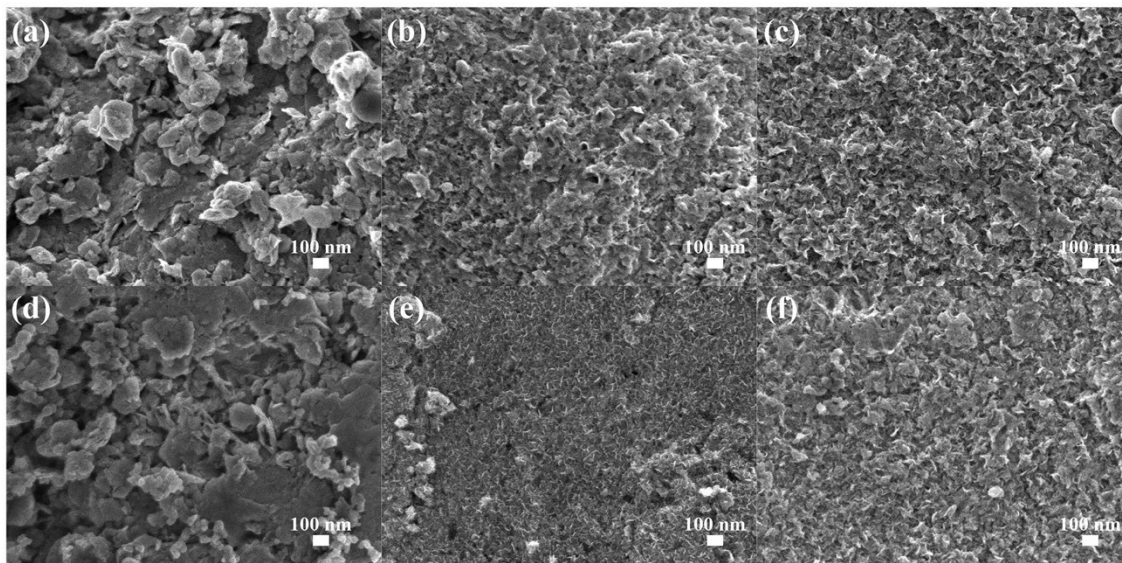


Figure S13. FE-SEM images of the pristine birnessite-type layered manganese oxide (δ - MnO_x) electrodes; (a) Li-MnO_x , (b) Na-MnO_x , (c) K-MnO_x , as well as the birnessite-type layered manganese oxide after 100 cycles of CV test at 10 mV s^{-1} ; (d) Li-MnO_x , (e) Na-MnO_x , (f) K-MnO_x .

In order to evaluate the morphology of the materials after electrochemical evaluation, the field emission-scanning electron microscopy (FE-SEM) technique was utilized after cyclic voltammetry (CV) for 100 cycles. After the electrode fabrication process, all the birnessite manganese oxides become more compact but can still retain their sheet-like morphologies as displayed in Figure S13a-c. After CV test at 10 mV s^{-1} for 100 cycles, the morphologies of Li-MnO_x , Na-MnO_x , and K-MnO_x are shown in Figure S13d-f, respectively. No significant change was observed after the 100 cycles of CV as the sheet-like structure is retained, which could further confirm the electrochemical stability of birnessite manganese oxides upon the charging-discharging process.

Table S1. E₀ and Mn valent states derived from *in situ* Mn K-edge XANES spectra.

Sample	Applied potential	Absorption threshold energy (eV)	Mn oxidation state
Li-MnO _x	-	6549.36	3.27695128
Na-MnO _x	-	6549.15	3.22405795
K-MnO _x	-	6548.97	3.17872081
Li-MnO _x	-0.1 V vs. SCE	6549.35	3.27443255
	0.8 V vs. SCE	6551.37	3.78321601
	-0.1 V vs. SCE return	6549.36	3.27695128
Na-MnO _x	-0.1 V vs. SCE	6549.15	3.22405795
	0.8 V vs. SCE	6550.74	3.62453602
	-0.1 V vs. SCE return	6549.16	3.22657668
K-MnO _x	-0.1 V vs. SCE	6548.96	3.17620208
	0.8 V vs. SCE	6550.19	3.48600587
	-0.1 V vs. SCE return	6548.97	3.17872081

Table S2. The ratio between structural cation to Mn of the as-prepared Li-MnO_x, Na-MnO_x, and K-MnO_x as well as after 100 cycles of CV

Sample	C:Mn Ratio (C=Li ⁺ /Na ⁺ /K ⁺)	Na ⁺ :Mn Ratio
Li-MnO _x	0.310	-
Li-MnO _x (after cycled)	0.086	0.719
Na-MnO _x	0.375	0.375
Na-MnO _x (after cycled)	0.399	0.399
K-MnO _x	0.397	-
K-MnO _x (after cycled)	0.329	0.455

References

1. Q. Feng, K. Yanagisawa and N. Yamasaki, *J. Ceram. Soc. Jpn.*, 1996, **104**, 897-899.
2. Q. Feng, K. Yanagisawa and N. Yamasaki *J. Mater. Sci. Lett.*, 1997, **16**, 110-112.
3. J. K. McDonough, A. I. Frolov, V. Presser, J. Niu, C. H. Miller, T. Ubieta, M. V. Fedorov and Y. Gogotsi, *Carbon*, 2012, **50**, 3298-3309.
4. F. Béguin, V. Presser, A. Balducci and E. Frackowiak, *Adv. Mater.*, 2014, **26**, 2219-2251.
5. J. Yang, M. R. Jo, M. Kang, Y. S. Huh, H. Jung and Y.-M. Kang, *Carbon*, 2014, **73**, 106-113.
6. Y. Lu, X. Liu, W. Wang, J. Cheng, H. Yan, C. Tang, J.-K. Kim and Y. Luo, *Sci. Rep.*, 2015, **5**, 16584.

7. A. Singh and A. Chandra, *Sci. Rep.*, 2015, **5**, 15551.
8. N. Berton, M. Brachet, F. Thissandier, J. Le Bideau, P. Gentile, G. Bidan, T. Brousse and S. Sadki, *Electrochem. Commun.*, 2014, **41**, 31-34.
9. N. Phattharasupakun, J. Wutthiprom, P. Chiochan, P. Suktha, M. Suksomboon, S. Kalasina and M. Sawangphruk, *Chem. Commun.*, 2016, **52**, 2585-2588.
10. V. Ganesh, S. Pitchumani and V. Lakshminarayanan, *J. Power Sources*, 2006, **158**, 1523-1532.
11. V. Augustyn, P. Simon and B. Dunn, *Energ. Environ. Sci.*, 2014, **7**, 1597-1614.
12. H. Yin, C. Song, Y. Wang, S. Li, M. Zeng, Z. Zhang, Z. Zhu and K. Yu, *Electrochim. Acta*, 2013, **111**, 762-770.
13. T. Brezesinski, J. Wang, J. Polleux, B. Dunn and S. H. Tolbert, *J. Am. Chem. Soc.*, 2009, **131**, 1802-1809.
14. T. Brezesinski, J. Wang, S. H. Tolbert and B. Dunn, *Nat. Mater.*, 2010, **9**, 146-151.
15. T. C. Liu, W. Pell, B. Conway and S. Roberson, *J. Electrochem. Soc.*, 1998, **145**, 1882-1888.
16. P. Iamprasertkun, C. Tangarnjanavalukul, A. Krittayavathananon, J. Khuntilo, N. Chanlek, P. Kidkhunthod and M. Sawangphruk, *Electrochim. Acta*, 2017, **249**, 26-32.
17. P. Iamprasertkun, A. Krittayavathananon, A. Seubsai, N. Chanlek, P. Kidkhunthod, W. Sangthong, S. Maensiri, R. Yimnirun, S. Nilmoung, P. Pannopard, S. Ittisanronnachai, K. Kongpatpanich, J. Limtrakul and M. Sawangphruk, *Sci. Rep.*, 2016, **6**, 37560.
18. A. Krittayavathananon, T. Pettong, P. Kidkhunthod and M. Sawangphruk, *Electrochim. Acta*, 2017, **285**, 1008-1015.
19. T. Pettong, P. Iamprasertkun, A. Krittayavathananon, P. Sukha, P. Sirisinudomkit, A. Seubsai, M. Chareonpanich, P. Kongkachuichay, J. Limtrakul and M. Sawangphruk, *ACS Appl. Mater. Interfaces*, 2016, **8**, 34045-34053.
20. S. Daengsakul, P. Kidkhunthod, O. Soisang, T. Kuenoon, A. Bootchanont and S. Maensiri, *Microelectron. Eng.*, 2015, **146**, 38-42.
21. J.-K. Chang, M.-T. Lee, W.-T. Tsai, M.-J. Deng and I. W. Sun, *Chem. Mater.*, 2009, **21**, 2688-2695.
22. C. A. Beasley, M. B. Sassin and J. W. Long, *J. Electrochem. Soc.*, 2015, **162**, A5060-A5064.
23. G. Sauerbrey, *Z. Phys.*, 1959, **155**, 206-222.
24. J. Jiang and A. Kucernak, *Electrochim. Acta*, 2002, **47**, 2381-2386.
25. C. Julien, M. Massot, R. Baddour-Hadjean, S. Franger, S. Bach and J. P. Pereira-Ramos, *Solid State Ion.*, 2003, **159**, 345-356.
26. Y.-K. Hsu, Y.-C. Chen, Y.-G. Lin, L.-C. Chen and K.-H. Chen, *Chem. Commun.*, 2011, **47**, 1252-1254.

27. R. Palm, H. Kurig, K. Tõnurist, A. Jänes and E. Lust, *J. Electrochem. Soc.*, 2013, **160**, A1741-A1745.